

A Spectral Parameterization of Drag, Eddy Diffusion, and Wave Heating for a Three-Dimensional Flow Induced by Breaking Gravity Waves

XUN ZHU, JENG-HWA YEE, WILLIAM H. SWARTZ, AND ELSAYED R. TALAAT

Applied Physics Laboratory, The Johns Hopkins University, Baltimore, Maryland

LAWRENCE COY

U.S. Naval Research Laboratory, Washington, D.C.

(Manuscript received 31 August 2009, in final form 23 March 2010)

ABSTRACT

There are three distinct processes by which upward-propagating gravity waves influence the large-scale dynamics and energetics of the middle atmosphere: (i) nonlocalized transport of momentum through wave propagation in three dimensions that remotely redistributes atmospheric momentum in both zonal and meridional directions from wave generation to wave dissipation regions; (ii) localized diffusive transport of momentum, heat, and tracers due to mixing induced by wave breaking; and (iii) localized transport of heat by perturbing wave structures due to dissipation that redistributes the thermal energy within a finite domain. These effects become most significant for breaking waves when momentum drag, eddy diffusion, and wave heating—the “breaking trinity”—are all imposed on the background state. This paper develops a 3D parameterization scheme that self-consistently includes the breaking trinity in large-scale numerical models. The 3D parameterization scheme is developed based on the general relationship between the wave action flux and the subgrid-scale momentum and heat fluxes developed by Zhu in 1987 and a mapping approximation between the wave source spectrum and momentum deposition distribution developed by Alexander and Dunkerton in 1999. For a set of given input wind and temperature profiles at each model grid, the parameterization scheme outputs the vertical profiles of the subgrid-scale force terms together with the eddy diffusion coefficients in the momentum and energy equations for a 3D background flow.

1. Introduction

Three-dimensional (3D) numerical models are important tools used in the quantitative study of the middle atmosphere and interpretation of satellite measurements. Well-designed numerical models in the middle atmosphere often consist of several types of comprehensive modules representing radiation, dynamics, photochemistry, and transport. Among these four types of modules, the dynamics or the dynamical core of a numerical model plays a critical role in organizing and coupling different physical processes in a consistent manner. This is mainly due to the dynamics being controlled by fluid mechanics that is a continuum, behaving highly nonlinearly, and evolving with time on many different scales. The other

modules play complementary roles. For example, the physics module for calculating radiative heating and photolysis rates provides the parameterized force to drive the dynamics and photochemistry. This partially affects the dynamics with bounded or controllable uncertainty because the time-independent problem of radiative transfer is well defined and solvable for a given input of atmospheric parameters, such as temperature and species, solar irradiance spectrum, and kinetics database (e.g., Zhu 2004; Mlynczak and Zhou 1998; Zhu et al. 2007). From the perspective of satellite measurements and the global modeling of atmospheric structure, it is often the large-scale dynamics and transport that can be observed directly with instruments and simulated explicitly with models. For example, tidal winds were directly observed from the Upper Atmosphere Research Satellite High Resolution Doppler Imager (UARS/HRDI) and were used to estimate the momentum deposition based on the derived velocity correlation terms that characterize the effect of tides on the zonal mean flow (Lieberman

Corresponding author address: Dr. Xun Zhu, The Johns Hopkins University, Applied Physics Laboratory, 11100 Johns Hopkins Road, Laurel, MD 20723–6099.
E-mail: xun.zhu@jhuapl.edu

Report Documentation Page

Form Approved
OMB No. 0704-0188

Public reporting burden for the collection of information is estimated to average 1 hour per response, including the time for reviewing instructions, searching existing data sources, gathering and maintaining the data needed, and completing and reviewing the collection of information. Send comments regarding this burden estimate or any other aspect of this collection of information, including suggestions for reducing this burden, to Washington Headquarters Services, Directorate for Information Operations and Reports, 1215 Jefferson Davis Highway, Suite 1204, Arlington VA 22202-4302. Respondents should be aware that notwithstanding any other provision of law, no person shall be subject to a penalty for failing to comply with a collection of information if it does not display a currently valid OMB control number.

1. REPORT DATE MAR 2010	2. REPORT TYPE	3. DATES COVERED 00-00-2010 to 00-00-2010	
4. TITLE AND SUBTITLE A Spectral Parameterization of Drag, Eddy Diffusion, and Wave Heating for a Three-Dimensional Flow Induced by Breaking Gravity Waves		5a. CONTRACT NUMBER	
		5b. GRANT NUMBER	
		5c. PROGRAM ELEMENT NUMBER	
6. AUTHOR(S)		5d. PROJECT NUMBER	
		5e. TASK NUMBER	
		5f. WORK UNIT NUMBER	
7. PERFORMING ORGANIZATION NAME(S) AND ADDRESS(ES) Naval Research Laboratory, Washington, DC, 20375		8. PERFORMING ORGANIZATION REPORT NUMBER	
9. SPONSORING/MONITORING AGENCY NAME(S) AND ADDRESS(ES)		10. SPONSOR/MONITOR'S ACRONYM(S)	
		11. SPONSOR/MONITOR'S REPORT NUMBER(S)	
12. DISTRIBUTION/AVAILABILITY STATEMENT Approved for public release; distribution unlimited			
13. SUPPLEMENTARY NOTES			
14. ABSTRACT There are three distinct processes by which upward-propagating gravity waves influence the large-scale dynamics and energetics of the middle atmosphere: (i) nonlocalized transport of momentum through wave propagation in three dimensions that remotely redistributes atmospheric momentum in both zonal and meridional directions from wave generation to wave dissipation regions; (ii) localized diffusive transport of momentum, heat, and tracers due to mixing induced by wave breaking; and (iii) localized transport of heat by perturbing wave structures due to dissipation that redistributes the thermal energy within a finite domain. These effects become most significant for breaking waves when momentum drag, eddy diffusion, and wave heating? the ??breaking trinity???are all imposed on the background state. This paper develops a 3D parameterization scheme that self-consistently includes the breaking trinity in large-scale numerical models. The 3D parameterization scheme is developed based on the general relationship between the wave action flux and the subgrid-scale momentum and heat fluxes developed by Zhu in 1987 and a mapping approximation between the wave source spectrum and momentum deposition distribution developed by Alexander and Dunkerton in 1999. For a set of given input wind and temperature profiles at each model grid, the parameterization scheme outputs the vertical profiles of the subgrid-scale force terms together with the eddy diffusion coefficients in the momentum and energy equations for a 3D background flow.			
15. SUBJECT TERMS			
16. SECURITY CLASSIFICATION OF:			17. LIMITATION OF ABSTRACT Same as Report (SAR)
a. REPORT unclassified	b. ABSTRACT unclassified	c. THIS PAGE unclassified	
19a. NAME OF RESPONSIBLE PERSON			

and Hays 1994). The temperature measured from the Sounding of the Atmosphere using Broadband Emission Radiometer (SABER) onboard the *Thermosphere, Ionosphere, Mesosphere, Energetics and Dynamics (TIMED)* satellite has been used to derive planetary-scale waves for both temperature and winds and the associated wave force terms such as the Eliassen–Palm flux divergence of tides in the middle atmosphere (Zhu et al. 2005, 2008). These large-scale fields derived from satellite observations can be directly assimilated into numerical models in a diagnostic analysis to gain additional physical insights into middle atmosphere dynamics (e.g., Akmaev 1997; Zhu et al. 2005). On the other hand, the momentum and energy sources produced by subgrid-scale motions have to be parameterized.

For middle atmospheric modeling studies, the subgrid-scale motions can be most effectively represented by gravity waves because of their ability to transport momentum and energy over a large spatial distance. Generated mainly in the troposphere by mechanisms such as flow over topography (e.g., Nappo 2002; Teixeira et al. 2004), convection (e.g., Alexander et al. 1995), shear instability (e.g., Lindzen 1974; Scinocca and Ford 2000), and geostrophic adjustment (e.g., Zhu and Holton 1987), gravity waves can propagate upward into the mesosphere and lower thermosphere (MLT) (e.g., Hines 1960). It has been well established that *zonal* forces generated by breaking gravity waves are crucial to maintain large-scale dynamics and transport in the middle atmosphere, especially in the MLT region (e.g., Lindzen 1981; Holton 1983; Fritts 1984; Holton and Zhu 1984; McIntyre 2000; Holton and Alexander 2000). It is also known, both observationally and theoretically, that wave generation and propagation are 3D in space (e.g., Fritts 1984, 1995; Zhu 1987; Sato 1994; Marks and Eckermann 1995; Broutman et al. 2001, 2002, 2004). On a slowly varying time scale or averaged over a wave period, a propagating gravity wave will not have any effect on the background wind or temperature unless the wave is subject to dissipation in wave action (e.g., Lighthill 1978; Zhu 1987; Eckermann 1992). On the other hand, a dissipative wave could (i) induce a momentum drag on the background flow, (ii) produce eddy mixing in the background dynamical and tracer fields, and (iii) generate a heating–cooling dipole on the background temperature field. The mechanisms that contribute to the dissipation of a gravity wave disturbance in the middle atmosphere are convective and dynamical instabilities, radiative damping, eddy diffusion, and nonlinear wave–wave interactions. In the lower thermosphere, molecular diffusion makes an additional contribution. Among these dissipative processes, the convective and dynamical instabilities associated with wave breaking are believed to be dominant in producing

momentum drag and eddy diffusion in the background flow (Fritts and Rastogi 1985). This is mainly because the characteristic gravity waves in the middle atmosphere are of high frequency and long vertical wavelength (e.g., Hirota and Niki 1985; Zhu et al. 1997), such that they can propagate over a large distance without significant damping before wave breaking. In addition to the drag and eddy diffusion that have been extensively studied and have been parameterized in many middle atmosphere models, it has been recognized recently that the dynamical heating associated with the downward heat flux by dissipative gravity waves also needs to be included in middle atmosphere models (Becker 2004; Akmaev 2007). Based on the rocket measurements of neutral density fluctuations, Lübken (1997) found that the dynamical heating rate near the mesopause estimated from the turbulence energy dissipation rates amounts to 10–20 K day⁻¹, which is comparable to the magnitudes of radiative and chemical heating rates in the same region. In summary, the most effective dissipation of gravity waves—wave breaking—produces three important effects on the background state: wave drag, eddy diffusion, and wave heating. Here, we call these three dynamical and energetic consequences resulting from gravity wave breaking in the middle atmosphere the “breaking trinity.”

In terms of momentum flux or Reynolds stresses, the parameterization of subgrid-scale motions by gravity waves is fundamentally different from those in so-called turbulent viscosity models, where the Reynolds stresses are essentially parameterized by various length theories, including Prandtl’s mixing-length theory and *K*-epsilon models (e.g., Tennekes and Lumley 1972; Pope 2000). In the latter case, the momentum is carried and transferred by moving fluid parcels for a localized exchange. For mechanistic general circulation models (GCMs) with a high resolution that can explicitly resolve medium-scale gravity waves, the localized mixing-length theory can also be adopted to parameterize the effects of eddies with much smaller subgrid scales (Becker 2009). On the other hand, gravity waves carry and transfer momentum by pressure and velocity fluctuations over a large spatial distance. Such a nonlocalized transport of momentum also provides one of the important physical bases for changes in the tropospheric circulation to affect the MLT dynamics and climatology. From the perspective of wave–mean flow interactions in 3D flow on how the momentum and energy are spatially redistributed within the entire domain, the breaking trinity can be understood as three effects of wave propagation and dissipation on the 3D mean flow: (i) nonlocalized transport of momentum through wave propagation in 3D that remotely redistributes atmospheric momentum in both

zonal and meridional directions from wave generation to wave dissipation regions; (ii) localized diffusive transport of momentum, heat, and tracers due to 3D mixing induced by wave breaking; and (iii) localized transport of heat by perturbing wave structures that redistributes the thermal energy within a finite domain. To quantitatively and self-consistently examine these effects on the 3D background state, we need a parameterization scheme that can provide (i) wave drag to the background 3D flow consisting of both the zonal and meridional components in the momentum equations, (ii) eddy diffusion to the dynamical and tracer fields that represents the mixing or the field smoothness by parameterized subgrid-scale motions, and (iii) wave heating to the temperature field induced by the wave breaking in the energy equation, all resulting from the dissipation of wave action caused by the interaction between 3D subgrid-scale waves and 3D background flow. This paper introduces a new parameterization scheme of drag, eddy diffusion, and wave heating imposed on a 3D background state by the breaking of gravity waves. The output of the new parameterization scheme will self-consistently include all three distinct processes associated with the breaking trinity by which the upward-propagating gravity waves influence the 3D large-scale dynamics and energetics of the middle atmosphere.

In section 2, we introduce a spectral parameterization scheme of gravity wave breaking that simultaneously produces the breaking trinity for given 3D wind and temperature profiles. The central part of the derivation is built on previous work by Holton and Zhu (1984), Zhu (1987), and Alexander and Dunkerton (1999), which was based on the general relationship between the wave action flux and the wave momentum, and also on a simple mapping approximation between the wave source spectrum in wave parameters and momentum deposition distribution in altitude. Section 3 shows the typical magnitudes and patterns of the breaking trinity to a 3D background field of wind and temperature derived from an output field of a high-altitude version of the Goddard Earth Observing System atmospheric model (GEOS-5). Finally, section 4 summarizes the paper.

2. Parameterization of gravity wave breaking in a three-dimensional background flow

a. Wave-mean flow interaction in a three-dimensional atmosphere

Following Holton (1975) and Zhu (1987), the gravity wave-mean flow interactions in a 3D atmosphere are described by two sets of coupled equations. One is for the large-scale and slowly varying background flow,

which can be resolved explicitly by the model grid, and the other is for 3D wave fields. For simplicity and also because the effects of the breaking trinity due to the subgrid-scale motions will be parameterized at each model grid independently, we develop our parameterization scheme by assuming the hydrostatic approximation on an f plane. Using the two-scale analysis method, the equations for the evolution of a background state under a localized wave forcing representing the subgrid-scale motions can be written as (Holton 1975; Zhu 1987)

$$\overline{D}\overline{u} - f\overline{v} + \frac{\partial\overline{\Phi}}{\partial x} = S_u + \frac{\partial}{\partial z}\left(K_{zz-m}\frac{\partial\overline{u}}{\partial z}\right), \quad (1)$$

$$\overline{D}\overline{v} + f\overline{u} + \frac{\partial\overline{\Phi}}{\partial y} = S_v + \frac{\partial}{\partial z}\left(K_{zz-m}\frac{\partial\overline{v}}{\partial z}\right), \quad (2)$$

$$\overline{D}\left(\frac{\partial\overline{\Phi}}{\partial z}\right) + N^2\overline{w} = S_T + \frac{\partial}{\partial z}\left(K_{zz-T}\frac{\partial^2\overline{\Phi}}{\partial z^2}\right), \quad (3)$$

with

$$S_u = \frac{-1}{\rho_0}\mathbf{V}\cdot\mathbf{F}_u, \quad S_v = \frac{-1}{\rho_0}\mathbf{V}\cdot\mathbf{F}_v, \quad S_T = \frac{-1}{\rho_0}\mathbf{V}\cdot\mathbf{F}_{\Phi_z}. \quad (4a,b,c)$$

In the above equations, \overline{u} , \overline{v} , and \overline{w} are the background zonal x , meridional y , and vertical z velocities, respectively; $\overline{\Phi}$ is the background geopotential and is hydrostatically related to the background temperature \overline{T} ; f is the Coriolis parameter; ρ_0 is the background density of the atmosphere; N^2 is the squared buoyancy frequency; and \overline{D} is the time derivative following the horizontal component of the background wind:

$$\overline{D} = \frac{\partial}{\partial t} + \overline{u}\frac{\partial}{\partial x} + \overline{v}\frac{\partial}{\partial y}. \quad (5)$$

The squared buoyancy frequency slowly varies with altitude and is a measure of the static stability of the background atmosphere:

$$N^2(z) = \frac{R}{H}\left(\frac{\partial\overline{T}}{\partial z} + \frac{\kappa\overline{T}}{H}\right), \quad (6)$$

where R is the gas constant, H is the scale height of the background air density, $\kappa \equiv R/c_p \approx 2/7$, and c_p is the specific heat at constant pressure. The left-hand sides of Eqs. (1)–(3) represent the dynamical evolution of a flow on a grid-resolved scale. The dynamical cores of different GCMs may differ significantly. The right-hand terms in Eqs. (1)–(3) represent the momentum and energy

sources contributed by the nonconservative processes of dissipation and transience of upward-propagating subgrid-scale gravity waves, (S_u, S_v) and S_T are the wave drag and heating terms, and K_{zz-m} and K_{zz-T} are the eddy diffusion coefficients for the momentum and sensible heat, respectively. Note that K_{zz-m} and K_{zz-T} are related by the eddy Prandtl number $P_r (= K_{zz-m}/K_{zz-T})$. Since the sensible heat flux is proportional to the potential temperature gradient, K_{zz-T} can also be used for parameterizing subgrid-scale chemical tracer transport. In Eq. (4), $(\mathbf{F}_u, \mathbf{F}_v)$ and \mathbf{F}_{ϕ_z} are the pseudomomentum flux and sensible heat flux, respectively. In this paper, all these terms and coefficients are calculated for a spectral distribution of a set of upward-propagating gravity waves specified at the wave source region in the lower atmosphere. Computationally, a subroutine that uses the vertical wind and temperature profiles as input at each model grid returns five vertical profiles of S_u , S_v , S_T , K_{zz-m} , and K_{zz-T} in Eqs. (1)–(3). In addition, the geographic location and seasonal timing also determine the statistical properties of the source spectrum for the gravity waves specified in the lower atmosphere.

In Eqs. (1)–(3), the momentum ($\rho_0 u$, $\rho_0 v$) and total potential energy ($\rho_0 c_p T$) under the Boussinesq approximation are all linear variables, so the eddy forcing terms on the right-hand sides of the mean momentum and energy equations can all be expressed in flux form, as shown in Eq. (4) (Holton 1975). As a result, the mean momentum and potential energies can be spatially redistributed through the flux divergences, but the integrations over an enclosed domain will be solely determined by the boundary fluxes. Mathematically, this is also because the average of a perturbed linear quantity vanishes (e.g., $\overline{\rho_0 u'} = 0$) so the eddy terms do not contribute to the mean quantities in the volume integrations. Some parameterization schemes for gravity wave breaking have been developed based on an energy equation that also includes the kinetic energy (e.g., Becker 2004). Since the kinetic energy is a quadratic quantity, the separation of the atmospheric motion between the mean and eddies will result in two nonzero terms in its kinetic energy (e.g., $\overline{\rho_0 u^2} = \rho_0 \overline{u^2} + \rho_0 \overline{u'^2}$). In this case, the mean energy equation can no longer be written in a purely flux form because there exists an energy conversion between the mean and eddy fields. Furthermore, when the kinetic energy is to be explicitly included in the energy budget, a more sensible approach is to introduce the available potential energy that is also quadratic in temperature (Lorenz 1955). Under such a circumstance, only the total energy that includes both the mean plus eddy and kinetic plus available potential energies is still conserved and can be written in a purely flux form (e.g., Dutton 1976; Holton 1975).

The effect of the background state on a wave component is described by a set of ray tracing equations in a 3D stratified flow for its wave parameters (e.g., Lighthill 1978; Zhu 1987; Marks and Eckermann 1995; Broutman et al. 2004). Specifically, the wave amplitude is best described by the wave action conservation law

$$\frac{\partial A}{\partial t} + \nabla \cdot (\mathbf{c}_g A) = -\alpha_w A, \quad (7)$$

where $A = E/\hat{\omega}$ is the wave action density, with E and $\hat{\omega}$ being the wave energy density and intrinsic frequency, respectively; \mathbf{c}_g is the group velocity and $\mathbf{c}_g A$ is called the wave action flux; and α_w is the bulk damping rate coefficient of the wave component, which characterizes various damping processes including radiative and eddy diffusive damping, molecular diffusion, and wave breaking. A wave component is also called a wave packet if its wave parameters vary slowly with space and time. The interaction between a wave packet and the background mean flow is often expressed by a relationship between the wave action flux and pseudomomentum flux or Eliassen–Palm flux (e.g., Dunkerton 1981; Palmer 1982; Andrews et al. 1987; Alexander and Dunkerton 1999). Given such a relationship, one can calculate the subgrid-scale drag terms in Eq. (4) once the wave action density has been solved from the wave action conservation law (7). Since the drag terms and dynamical heating term in Eqs. (1)–(4) have been expressed in flux form, the conservations of momentum and thermal energy of the dynamical core are automatically preserved for the grid-resolved flow as long as no spurious sources are introduced on the boundaries. Most models assume a hydrostatic approximation for both large-scale background state and subgrid-scale wave fields. Recently, Shaw and Shepherd (2009) proposed a framework to couple a hydrostatic large-scale flow to a nonhydrostatic subgrid-scale flow that preserves the momentum and total energy conservations self-consistently.

Assuming the background state and wave parameters are slowly varying in time and space with small dissipation, neglecting the effect of planetary rotation on medium-scale gravity waves, and using the two-scale analysis method, Zhu (1987) showed that the wave action density and the pseudomomentum and sensible heat fluxes in the first-order approximation for an individual gravity wave packet in Eqs. (1)–(4) were related through

$$\mathbf{F}_u = k \hat{\mathbf{c}}_g A, \quad \mathbf{F}_v = l \hat{\mathbf{c}}_g A, \quad \mathbf{F}_{\phi_z} = 0, \quad (8a,b,c)$$

where k and l are the horizontal wavenumbers of the wave packet in the x and y directions, respectively.

$\hat{\mathbf{c}}_g = \mathbf{c}_g - (\bar{u}, \bar{v}, 0)$ is the intrinsic group velocity Doppler-shifted by the horizontal component of the background wind. Equation (8) together with Eqs. (1)–(4) describe the effect of a wave packet on the background state. Note that since we have applied the hydrostatic and the f -plane approximations to the original set of equations there is no velocity shift in the vertical component of the group velocity, although it varies with altitude: $\hat{c}_{gz} = c_{gz}(z)$. The wave dispersion relation and c_{gz} under the hydrostatic approximation are given by (Zhu 1987)

$$\hat{\omega}^2 = f^2 + \frac{K^2 N^2}{\lambda^2 + 0.25/H^2}, \quad (9)$$

$$c_{gz} = -\frac{\lambda K^2 N^2}{\hat{\omega}(\lambda^2 + 0.25/H^2)}, \quad (10)$$

where λ is the vertical wavenumber and K is the total horizontal wavenumber defined by $K^2 = k^2 + l^2$. The inertial effect of the Coriolis parameter f in Eq. (9) becomes important only if one focuses on large-scale gravity waves with horizontal wavelengths of several hundred kilometers and examines their effects on lateral propagations (e.g., Dunkerton 1984). Since our parameterization scheme is to be implemented on each model grid independently, the inertial effect is often neglected in the current paper except when its effect becomes important in prescribing wave parameters. Also note that the sensible heat flux vanishes under the first-order approximation for a conservative gravity wave component, as shown above in Eq. (8c). Equation (8) shows that for a given wave action flux $\hat{\mathbf{c}}_g A$ that has been shifted by the background wind the ratio of the momentum fluxes between x and y directions is related by the direction of the wavenumber vector (k, l) and is independent of the direction of the background flow vector $[\bar{u}(z), \bar{v}(z)]$. This means that the partition of the pseudomomentum flux vector between x and y directions is determined by the wave structure. The same dependent relations of the momentum flux on the wavenumber vector and wave action density were also derived by Warner and McIntyre (1996) in their extension of Lindzen's (1981) parameterization scheme, where the distribution and variation of the energy spectrum were prescribed in terms of λ . Assuming a steady vertical wind profile that is slowly varying in the horizontal direction, it can be shown that the horizontal wavenumber (k, l) and the ground-relative wave frequency ω do not vary with altitude (e.g., Zhu 1987; Eckermann 1992). Therefore, the partition between \mathbf{F}_u and \mathbf{F}_v of a wave component is entirely determined by its horizontal wave vector specified at the source region. Furthermore, since the horizontal components of the

phase velocity $(c_x, c_y) = (\omega/k, \omega/l)$ do not vary with altitude either, most parameterization schemes have specified the source spectra as a function of (k, l) and phase speed c at the lower boundary (e.g., Holton and Zhu 1984; Alexander and Dunkerton 1999; Becker and Schmitz 2002). Such a dependence on wave parameters in prescribing the wave spectrum at the source region will also be adopted in the current parameterization scheme.

The wave action conservation law (7) suggests that the wave action flux ($\mathbf{c}_g A$) is a conserved quantity in the absence of wave dissipation ($\alpha_w = 0$). As a result, A is invariant and its value along the rays depicted by \mathbf{c}_g is a constant regardless of how other individual wave parameters vary as the wave packet interacts with the background state. Specifically, assuming the steady-state approximation ($\partial/\partial t = 0$), the wave action flux $\mathbf{c}_g A$ at two different cross sections in space will be identical and thus can be evaluated easily. On the other hand, the pseudomomentum fluxes in Eq. (8) associated with the drag terms in Eqs. (1) and (2) contain the intrinsic group velocity, which prevents one from directly applying the wave action conservation law. However, for a parameterization scheme in the middle atmosphere that assumes the upward-propagating gravity waves are dominant, the momentum flux convergence is exclusively contributed from the vertical component of the pseudomomentum fluxes. Under such a circumstance, we have

$$\begin{aligned} F_{u,z} &= \cos\theta_0(Kc_{gz}A), & F_{v,z} &= \sin\theta_0(Kc_{gz}A), \\ F_{\phi_{z,z}} &= -\omega_i \hat{\omega} A, \end{aligned} \quad (11a,b,c)$$

where we have introduced the horizontal direction of wave propagation θ_0 based on the horizontal wavenumber vector by $(k, l) = K(\cos\theta_0, \sin\theta_0)$. We have also shown the higher-order approximation of the sensible heat flux in Eq. (11c), where $\hat{\omega}$ and ω_i are the real and imaginary parts of the intrinsic frequency, respectively (Holton and Zhu 1984). Equation (11) shows explicitly that for an upward-propagating ($c_{gz} > 0$) gravity wave packet the signs of the momentum flux components are determined by the wavenumber vector. Also, the dissipation ($\omega_i > 0$) induces a downward heat flux ($F_{\phi_{z,z}} \leq 0$) for an upward-propagating gravity wave that has a positive $\hat{\omega}$ by the notation convention (Holton and Zhu 1984).

Expressions similar to Eq. (11c) have also been derived previously (Walterscheid 1981; Talaat et al. 2001; Becker 2004). Here, for 3D applications that include both the zonal and meridional velocity components and also for using horizontal wavenumber and phase speed as working wave parameters, the intrinsic frequency is related to the ground-relative frequency ω by $\hat{\omega} = \omega - k\bar{u} - l\bar{v}$. If

we further define the direction of the background flow (\bar{u}, \bar{v}) by $U(\cos\delta, \sin\delta)$, then $\hat{\omega}$ can be simplified as

$$\hat{\omega} = \omega - KU \cos\theta = K(c - U \cos\theta), \quad (12)$$

where $U = \sqrt{\bar{u}^2 + \bar{v}^2}$ is the magnitude of the background flow and $\theta = \theta_0 - \delta$ is the angle between the horizontal wavenumber vector and background flow. Again, the ground-relative phase speed $c = \omega/K (>0)$ does not vary with altitude. The vertical sensible heat flux by the gravity wave component vanishes unless it is subject to damping or wave breaking that can be characterized by the imaginary part of its frequency ω_i . Note that it is the flux divergence that will contribute to the momentum and energy budgets in Eqs. (1)–(3). Furthermore, the flux form of Eq. (7) suggests that the internal damping and boundary values of wave action density are closely related. Hence, wave momentum and heat fluxes make similar types of contributions to the momentum and energy budgets in such a way that they only redistribute spatially within and vanish outside the dissipation and generation regions. Specifically, when the heat flux for a wave packet $F_{\phi_i, z}$ vanishes at both the lower boundary where waves are conserved ($\omega_i = 0$) and the upper boundary where all waves have been completely dissipated ($A = 0$), nonzero wave heating should occur in the form of a dipole so that the wave heating within a finite domain will be exactly balanced by wave cooling in an adjacent region. The wave damping associated with the breaking processes also leads to turbulent eddy diffusion that can be parameterized as eddy diffusion coefficients for the background state. Our parameterization scheme provides the breaking trinity, which includes both the momentum drag and sensible heating terms by wave breaking together with the eddy diffusion coefficients K_{zz-m} and K_{zz-T} used in Eqs. (1)–(3).

b. Extension of Lindzen's parameterization to a three-dimensional atmosphere

We have already indicated that the convective and dynamical instabilities associated with wave breaking are believed to be the dominant mechanism of wave dissipation for the upward-propagating gravity waves in the middle atmosphere. The wave breaking can produce both the momentum drag and eddy diffusion to the background flow (Lindzen 1981). On the other hand, for slowly propagating planetary waves where radiative damping is the main dissipation mechanism, the effect of eddy diffusion by wave dissipation on the background state is small and often neglected (e.g., Matsuno 1970; Holton and Lindzen 1972). Since ω_i represents the wave dissipation effect by either radiative damping or eddy

diffusion (Holton and Zhu 1984), the wave dynamical heating associated with Eq. (11c) remains potentially significant for a slowly propagating wave with radiative damping as its main dissipation mechanism. The instabilities of an upward-propagating gravity wave are mainly caused by the exponential growth of wave amplitude due to the atmospheric density effect or the increase of λ due to the critical level and are modified by the static stability of the background state. The most widely used parameterization schemes have been those based on Lindzen's (1981) theory of wave breaking and saturation. The term "saturation" refers to the growth cessation of an upward-propagating unstable wave component when its Richardson number reaches its critical value of $1/4$ (shear instability) or approaches zero (convective instability). Lindzen's parameterization scheme (1981) was originally proposed for deriving S_u and the associated K_{zz-m} for a zonal mean flow $(\bar{u}, 0)$. Although Lindzen's (1981) parameterization scheme was extended by Holton and Zhu (1984) and several others, most schemes only calculate four terms including S_u , K_{zz-m} , and K_{zz-T} in Eqs. (1)–(3) for a two-dimensional (2D) flow such as the one containing the x component of the wind profile. The central aspect in Lindzen's (1981) parameterization is that (i) the specification of the momentum deposition of the breaking wave component between the breaking level z_b and the critical level z_c is based on the saturation assumption. This original parameterization scheme was extended by Holton (1982) and Holton and Zhu (1984) in the following two aspects: (ii) a directional isotropic source spectrum of waves in phase speed is specified at the lower boundary and (iii) each wave component is influenced by Newtonian cooling and the eddy diffusion induced by the breaking of other wave components with lower z_b . Aspect (iii) allows the nonlinear interaction among different wave components to be partially included in the parameterization. These extensions also cause the wave momentum to be deposited in a more extended region of the atmosphere, especially below the dominant wave breaking level z_b . It is noted that aspects (i) and (iii) critically depend on aspect (ii), which varies with season and geography. In fact, all three key aspects rely on some approximations and include significant uncertainties. Furthermore, because of its relatively high frequency, the majority of the wave momentum for an upward-propagating gravity wave is deposited after its breakdown (i.e., in the region above its breaking level z_b).

Alexander and Dunkerton (1999) proposed a simplified version of Lindzen's parameterization scheme by neglecting the complex details of wave dissipation either below or above the breaking level z_b . They assumed all momentum of a wave component to be deposited at the

breaking level z_b . By doing so, they mathematically have directly mapped the source momentum spectrum in horizontal wavenumber and phase speed at the lower boundary to a momentum deposition and eddy diffusion coefficient in altitude. Such a simplified parameterization not only increases the efficiency of computation; more importantly, it also combines all the uncertainties in the above three aspects [(i)–(iii)] into one of specifying the source spectrum of the waves. In principle, this makes it much simpler to validate and improve the parameterization scheme as more observations of gravity wave variance and spectra become available. Furthermore, we will show below that such a simplification also makes the evaluation of the newly included sensible heat flux Eq. (11c) straightforward. The 3D parameterization scheme that includes the breaking trinity introduced below essentially combines the formulations of Holton and Zhu (1984), Zhu (1987), and Alexander and Dunkerton (1999) to give a set of output profiles of (S_u, S_v, S_T) and (K_{zz-m}, K_{zz-T}) as functions of altitude for a set of given input wind and temperature profiles of $(\bar{u}, \bar{v}, \bar{T})$ at each model grid.

From Zhu (1987), the wave energy density E for a 3D hydrostatic gravity wave packet is given by

$$E = \frac{\rho_{00} K^2 \Phi^2 \hat{\omega}^2}{2(\hat{\omega}^2 - f^2)^2}, \quad (13)$$

where ρ_{00} is the air density at the lower boundary z_0 and Φ is the geopotential. Assuming $f^2 \ll \hat{\omega}^2$ and neglecting the inertial effect in Eq. (13), we have the wave action density for a 3D gravity wave in a 3D background flow:

$$A = \frac{E}{\hat{\omega}} = \frac{\rho_{00} \Phi^2}{2K(c - U \cos\theta)^3}, \quad (14)$$

where we have used Eq. (12) to replace the wave frequency ω with the phase speed c . We note that the pseudomomentum flux F_p for a 2D model defined by Alexander and Dunkerton (1999) is equivalent to $\sqrt{\mathbf{F}_u^2 + \mathbf{F}_v^2}$ or $Kc_{gz}A$ in the present notation for a 3D model of gravity wave–mean flow interaction. Adopting the same approximation of $f^2 \ll \hat{\omega}^2$ in the dispersion relation (9) and further assuming $\lambda^2 \gg 0.25/H^2$ for breaking waves in Eqs. (9) and (10), we have

$$F_p = Kc_{gz}A = \frac{\rho_{00} K \Phi^2}{2N(c - U \cos\theta)}. \quad (15)$$

Equation (15) establishes a close connection between the momentum flux components in Eq. (11) and the wave parameters commonly observable and specified in most parameterization schemes.

Now, turning to Holton and Zhu (1984), the pseudomomentum flux of a 3D wave component in a 2D flow $[\bar{u}(z), 0]$ with buoyancy frequency $N(z)$ is given by

$$F_u \equiv \overline{\rho_0 u' w'} = \frac{\rho_{00} k \Phi_0^2 |c - \bar{u} \cos\theta_0|}{2N |c - \bar{u}_0 \cos\theta_0| (c - \bar{u} \cos\theta_0)} \times \exp\left(-2 \int_{z_0}^z \lambda_i dz\right), \quad (16)$$

where Φ_0 is the geopotential at the lower boundary z_0 , λ_i is the imaginary part of the vertical wavenumber, and the exponential factor in Eq. (16) represents the damping effect on the wave action. Note that both λ_i and ω_i represent the dissipation effect of a wave packet; their relationship is given by $\lambda_i \hat{\omega} = -\omega_i \lambda$, which can be derived by the dispersion relation (Holton and Zhu 1984). Also, the wave pseudomomentum flux is inversely proportional to the buoyancy frequency because waves are more easily amplified in a less statically stable atmosphere. At the lower boundary z_0 , where $\bar{u} = \bar{u}_0$, we have

$$F_{p0} \equiv (K/k)F_{u0} = \frac{\rho_{00} K \Phi_0^2}{2N(c - \bar{u}_0 \cos\theta_0)}. \quad (17)$$

Comparing Eq. (17) with Eq. (15) shows a great similarity between the two and also shows how a formulation for a 2D flow $[\bar{u}(z), 0]$ can be appropriately extended to a 3D flow. It is the magnitude of the background wind U and the wavenumber vector direction with respect to the background wind ($\theta = \theta_0 - \delta$) that matters formally. Specifically, if we follow a procedure similar to Holton and Zhu (1984) for a 3D flow $[\bar{u}(z), \bar{v}(z)]$, we can derive the condition for the determination of the breaking level z_b :

$$F_{p0} = \frac{\rho_0(z_b) K}{2N(z_b)} |c - U_b \cos\theta|^3 \frac{|c - U_0 \cos\theta|}{(c - U_0 \cos\theta)} \times \exp\left(2 \int_{z_0}^{z_b} \lambda_i dz\right), \quad (18)$$

where F_{p0} is given by Eq. (15) with $N = N_0$ and $U = U_0$; $N(z_b)$ and $\rho_0(z_b)$ are the background buoyancy frequency and air density at the breaking level, respectively. We have also assumed a slowly varying buoyancy frequency in this derivation.

At this stage, we follow Alexander and Dunkerton (1999) by neglecting any damping to gravity waves below the breaking level [i.e., setting $\lambda_i = 0$ in Eq. (18)]. Then, the condition for wave breaking is simplified to

$$\hat{c}_b \equiv c - U_b \cos\theta = \left[\frac{N_b \Phi_0^2}{N_0(c - U_0 \cos\theta)} \right]^{1/3} \exp\left(\frac{z_b - z_0}{3H}\right), \tag{19}$$

where \hat{c}_b is the breaking level intrinsic phase speed. Equation (19) is a direct extension of Eq. (6) in Alexander and Dunkerton (1999) to a 3D wave packet in a 3D atmosphere. It also defines the breaking level intrinsic frequency $\hat{\omega}_b = K\hat{c}_b$.

To examine how the breaking condition is satisfied, we rewrite the above equation at altitude z :

$$(c - U \cos\theta)(c - U_0 \cos\theta)^{1/3} [N_0/N(z)]^{1/3} = \Phi_0^{2/3} \exp\left(\frac{z - z_0}{3H}\right). \tag{20}$$

At the lower boundary z_0 , the left-hand side of Eq. (20) should be greater than the right-hand side:

$$(c - U_0 \cos\theta)^{4/3} > \Phi_0^{2/3}. \tag{21}$$

Wave components not satisfying the above condition at the lower boundary are unstable and will be eliminated from the source spectrum in the parameterization scheme (Alexander and Dunkerton 1999). Note that the left-hand side of Eq. (20) represents the effect of the critical level on wave amplitude, whereas the right-hand side of Eq. (20) is the amplification of the wave amplitude due to the atmospheric density effect. Also, the background stratification modifies the wave amplitude so that the pseudomomentum flux is inversely proportional to the buoyancy frequency as shown in Eq. (16). As z increases, the breaking condition (19) for an upward-propagating gravity wave in the absence of damping ($\lambda_i = \omega_i = 0$) can be satisfied through either the atmospheric density effect that increases the right-hand side of Eq. (20) exponentially or the effect of a critical level where the left-hand side of Eq. (20) greatly decreases as $U \cos\theta \rightarrow c$. Equation (20) also implies that the wave action density is strictly conserved below the breaking level z_b . Physically, this means that a wave breaks when it approaches a critical level of increasing lapse rate because of the increase of the vertical wavenumber and/or when its amplitude increases because of the decrease of the background air density. Furthermore, and most importantly, according to Eqs. (7) and (11) the pseudomomentum and sensible heat fluxes are constant before the wave reaches the breaking level: $F_P(z) = F_{P0}$ and $F_{\phi,z}(z) = 0$ for $z < z_b$ when $\lambda_i = \omega_i = 0$.

A complete dispersion relation for a nonhydrostatic inertia-gravity wave is given by (Marks and Eckermann 1995)

$$\hat{\omega}^2 \equiv (\omega - k\bar{u} - l\bar{v})^2 = \frac{f^2(\lambda^2 + 0.25/H^2) + N^2 K^2}{K^2 + \lambda^2 + 0.25/H^2}. \tag{22}$$

The hydrostatic dispersion relation Eq. (9) can be recovered from Eq. (22) by an approximation $K^2 \ll (\lambda^2 + 0.25/H^2)$ for large-scale waves, corresponding to a horizontal wavelength much greater than its characteristic vertical scale. Equation (22) explicitly shows that the squared intrinsic frequency $\hat{\omega}^2$ is the weighted average of two squared cutoff frequencies f^2 and N^2 . This leads to the following simplified condition for the permitted phase speed for the default setting of the parameters in the parameterization scheme:

$$\frac{f^2}{K^2} < (c - U \cos\theta)^2 < \frac{N^2}{K^2 + 0.25/H^2}, \tag{23}$$

where the Coriolis parameter f is a prescribed cutoff frequency for trapped waves at the lower boundary and $N = N(z)$ is the cutoff frequency for reflected waves at the entire altitude. Waves that do not satisfy Eq. (23) before encountering breaking levels will also be eliminated from the spectrum. Condition (23) is again a 3D extension of a similar condition of total internal reflection when $\hat{\omega}^2$ exceeds N^2 given by Alexander and Dunkerton (1999) and also the possible reflection by Jones' critical levels of $\hat{\omega}^2 = f^2$ (Yamanaka and Tanaka 1984) at the lower boundary. Computationally, we further set $|f| > 2 \times 10^{-5} \text{ s}^{-1}$ so that the left-side inequality of Eq. (23) excludes unusually large values of F_{P0} in specifying the source spectra based on Eq. (15) for a given Φ_0 field at the lower boundary.

For waves that reach breaking levels, we mainly follow Alexander and Dunkerton (1999) and assume that all the momentum is deposited at the breaking levels, producing the breaking trinity of momentum drag, eddy diffusion, and wave heating locally. Mathematically, the procedure is equivalent to mapping the source momentum spectrum in horizontal wavenumber and phase speed to a momentum deposition in altitude. Such a mapping procedure also makes the evaluation of Eq. (11c) straightforward. To illustrate this point explicitly, we rewrite Eq. (11c) as

$$F_{\phi,z} = -\left(\frac{\omega_i \hat{\omega}}{D_{zz} K c_{gz}}\right) D_{zz}(K c_{gz} A) \equiv -\Pi D_{zz}(K c_{gz} A), \tag{24}$$

where D_{zz} is the wave eddy diffusion coefficient at the breaking level z_b and is proportional to the momentum deposition rate for the breaking wave component (Holton 1982; Alexander and Dunkerton 1999):

$$D_{zz} = \sqrt{S_u^2 + S_v^2} (c - U \cos\theta) / N^2. \quad (25)$$

Below the breaking level, $F_{\phi, z}$ vanishes because $\omega_i = 0$ for a wave packet without dissipation. At $z = z_b$, $\omega_i = \lambda^2 D_{zz}$ (Lindzen 1981) so we have a nonzero heat flux once the wave starts breaking. Note that for a given horizontal wavenumber K , the intrinsic phase speed \hat{c}_b and frequency $\hat{\omega}_b$ at the breaking level are known and determined by Eq. (19). As a result, the corresponding λ and c_{gz} at z_b can also be easily calculated by the dispersion relations [Eqs. (9) and (10)]:

$$\lambda^2 \approx \frac{N^2}{\hat{c}_b^2}, \quad c_{gz} = \left| \frac{K^2 N^2}{\lambda^3 \hat{\omega}_b} \right|. \quad (26a, b)$$

Therefore, the coefficient defined in brackets in Eq. (24) can be expressed in known wave parameters: $\Pi = N^3 / (\hat{c}_b^3 K)$. In Eq. (26), we have again assumed λ to be much greater than $1/(2H)$ at z_b . This is a good approximation because waves generally break near critical levels where $\lambda^2 \gg (0.25/H^2)$. At this stage, all the flux

terms in Eqs. (11a)–(11c) can be simultaneously and self-consistently calculated once the pseudomomentum flux $Kc_{gz}A$ is specified at the lower boundary for a set of wave parameters. In the current notation, the induced breaking trinity of momentum drag, eddy diffusion coefficient, and wave heating rate at altitude z_k by breaking wave components ($j = 1, \dots, J$) can be calculated in the following formulations:

$$X_h = \frac{\varepsilon}{\rho_0(z_h)\Delta z} \sum_j (\cos\theta_0 F_{P0})_j \quad \text{for } z_{k-1} < z_b(c_j) \leq z_k, \quad (27)$$

$$Y_h = \frac{\varepsilon}{\rho_0(z_h)\Delta z} \sum_j (\sin\theta_0 F_{P0})_j \quad \text{for } z_{k-1} < z_b(c_j) \leq z_k, \quad (28)$$

$$D_h = \frac{\varepsilon_m \varepsilon}{\rho_0(z_h)N^2(z_h)\Delta z} \sum_j [c - U(z_h) \cos\theta]_j (F_{P0})_j \quad \text{for } z_{k-1} < z_b(c_j) \leq z_k, \quad (29)$$

$$Q_h = \begin{cases} \frac{\varepsilon^2}{\rho_0^2(z_h)N^2(z_h)\Delta z^2} \sum_j [c - U(z_h) \cos\theta]_j (\Pi F_{P0}^2)_j, & z_{k-1} < z \leq z_k \\ \frac{-\varepsilon^2 \rho_0^{-1}(z_{h+1})}{\rho_0(z_h)N^2(z_h)\Delta z^2} \sum_j [c - U(z_h) \cos\theta]_j (\Pi F_{P0}^2)_j, & z_k < z \leq z_{k+1} \end{cases}, \quad (30)$$

where $z_h = z_k - \Delta z/2$ and $z_{h-1} = z_k - \Delta z$ represent the half- and full-grid step below z_k , respectively. Outside the breaking regions as specified in the above expressions, the values are set to zero for those breaking waves. The force terms on the right-hand sides of Eqs. (1)–(3) on the model grids are the averages of the above expressions:

$$S_u(z_k) = \frac{1}{2}(X_h + X_{h+1}), \quad (31)$$

$$S_v(z_k) = \frac{1}{2}(Y_h + Y_{h+1}), \quad (32)$$

$$K_{zz-m}(z_k) = \frac{1}{2}(D_h + D_{h+1}), \quad (33)$$

$$K_{zz-T}(z_k) = K_{zz-m}(z_k)/P_r, \quad (34)$$

$$S_T(z_k) = \frac{1}{2}(Q_h + Q_{h+1}). \quad (35)$$

In the above equations, ε is an intermittency factor introduced by Alexander and Dunkerton (1999) that represents the ratio of the observed momentum flux to

the modeled one at the lower boundary. It is a specified parameter in the parameterization scheme that can vary with time, space, and wave parameters. The eddy diffusion coefficient derived from the Lindzen-type parameterization refers to the dissipation and momentum mixing to the wave field. To apply it to the background mean state, we introduce an additional parameter ε_m to characterize its efficiency for mixing the momentum of the background fields. Holton and Zhu (1984) showed that there was a partial cancellation between the direct wave drag and the drag induced by the eddy diffusion, which smoothed the total drag on the right-hand sides of Eqs. (1)–(3). The current parameterization scheme includes hundreds to thousands of wave components in the source spectrum, which yields smooth drag profiles for typical wind profiles. Therefore, we set a smaller value of $\varepsilon_m = 0.3$ in the current scheme. The eddy Prandtl number P_r is defined as the ratio of the eddy momentum diffusivity to the eddy heat and tracer diffusivity. It also reflects the fact that the wave eddy diffusion coefficient D_{zz} defined in Eq. (24) is different than the eddy diffusion coefficient for the background state K_{zz-m} defined in Eq. (33). Both

the mesospheric tracer measurements and careful model analysis of the breaking process show that P_r is much greater than 1 (e.g., Strobel et al. 1987; Strobel 1989; Chao and Schoeberl 1984). This is consistent with Eq. (8) of a vanishing sensible heat flux to a first-order approximation. We set $P_r = 5$ in the current scheme. Again, it is noted from Eqs. (27) and (28) that the partition of the deposited momentum in (x, y) direction is based neither on $(\cos\delta, \sin\delta)$ nor on $(\cos\theta, \sin\theta)$ but rather on $(\cos\theta_0, \sin\theta_0)$.

It should be pointed out that, strictly speaking, the first and second terms on the right-hand sides of Eqs. (1)–(3) represent two different ways of parameterizing the effects of subgrid-scale motions: nonlocalized wave forcing due to wave propagation and breaking versus localized mixing-length theory of turbulence. For a single gravity wave component, the wave-breaking processes occurring on scales much smaller than its wavelength dissipate the wave action and induce the explicit momentum and heat flux divergences shown in Eqs. (4) and (11). When there is a clear scale separation among the background grid-resolved motions, the smaller subgrid wave component, and a much smaller-scale mixing by wave breaking, the effect of the subgrid-scale eddy terms can be entirely included by the first terms (S_u, S_v, S_T) in Eqs. (1)–(3). Including the second eddy diffusion terms on the right-hand sides of Eqs. (1)–(3) implies that the vertical mixing by the much smaller-scale motions that directly dissipates the wave component also diffusively mixes the grid-resolved motions. The diffusion terms are expected to become more important as more gravity waves components with different wavelengths are included in the parameterization scheme because this will make the separation among different scales less obvious. This analysis also suggests that the additional parameter ε_m introduced in the current parameterization scheme is empirical and it may vary with the setting of the wave source spectrum.

From Eqs. (15), (19), (21), and (26), we see that, at z_b , \hat{c} and thus $\hat{\omega}$, F_{p0} , and Π are all positive. Therefore, the signs of the drag components are solely determined by the wavenumber vector direction $(\cos\theta_0, \sin\theta_0)$, whereas the heating rate and eddy diffusion coefficients are always positive. Previous studies (e.g., Walterscheid 1981; Liu 2000; Talaat et al. 2001) suggested that the gravity waves could induce dynamical cooling in the wave-dissipating region. A positive heating at z_b in the current parameterization scheme is mainly due to the assumption that each spectral wave component is completely dissipated at the breaking level where the wave heating occurs. On the other hand, if one assumes a finite and a broad region of wave dissipation between z_b and a higher level such as a critical level z_c where the wave amplitude completely vanishes, then cooling could occur in most

of the region between z_b and z_c . To accommodate such a cooling effect, we add a cooling term of the same magnitude in Eq. (30) immediately above z_b , which leads to a net effect of downward transport of heat near the wave breaking level. Physically, this means that there is no net heat being induced within the atmosphere when its vertical heat flux vanishes in both the lower and upper boundaries. Mathematically, the heat flux term of an upward-propagating gravity wave packet shown in Eq. (11c) experiences two major stages: (i) it changes from 0 to a finite value as the wave breaks because of a finite jump in ω_i at z_b and (ii) it changes back to 0 again as the wave approaches a critical level and completely dissipates so that $\hat{\omega}A \rightarrow 0$. Previous studies mainly focused on (ii) and overlooked (i). The net effect of Eq. (30), where the breaking waves heat the background atmosphere at z_b and cool it one level above z_b , is the downward transport of heat. We point out that the physical mechanism of this downward heat transport caused by a discontinuous wave breaking is slightly different from the same conclusion in previous studies (e.g., Walterscheid 1981), where the downward heat flux and the associated cooling only correspond to the above stage (ii).

Alexander and Dunkerton (1999) emphasized the dynamical importance of wave dissipation at z_b rather than at z_c . The above analysis of the heat flux and transport shows the energetic importance of wave dissipation at z_b . Wave dissipation at z_b produces a net downward transport of thermal energy to the mean state. Realization of $\omega_i = 0$ and $\hat{\omega}A = 0$ at the lower and upper boundaries respectively allows the finite downward heat transport to be evaluated self-consistently. This also makes Eq. (3) energetically consistent. In summary, the current parameterization of the breaking trinity extends the previous Lindzen types of parameterizations such as those by Holton and Zhu (1984) and Alexander and Dunkerton (1999) in two aspects: extending it to a 3D background flow and including a wave breaking-induced heating term. For a given set of input wind and temperature profiles $[u(z), v(z), T(z)]$ as a basic state in a model grid, the parameterization scheme of the breaking trinity outputs the vertical profiles of $(S_u, S_v, S_T, K_{zz-m}, K_{zz-T})$ that allow one to calculate all the force terms by the subgrid-scale motions such as those on the right-hand sides of Eqs. (1)–(3).

c. Specification of the source spectrum

A discrete source spectrum needs to be specified for the geopotential variance $\Phi_0^2(\theta_0, c, K)$ as a function of three wave parameters: θ_0 , c and K . We have already indicated the reason for choosing these three independent wave parameters for prescribing the wave spectrum: θ_0 , c , and K do not vary with altitude for an upward-propagating

wave component. In some parameterization schemes, such as the one by Warner and McIntyre (1996), the distribution and variation of the energy spectrum were prescribed as a function of λ and $\hat{\omega}$, both of which vary with the altitude. We assume a functional form that is separated in wavenumber vector direction: $\Phi_0^2(\theta_0, c, K) = B_1(\theta_0)B_2(c, K)$. Following Matsuno (1982) and Holton and Zhu (1984), we assume an isotropic distribution of Φ_0^2 in θ_0 [i.e., $B_1(\theta_0) = \bar{B} = \text{Constant}$]. Depending on specific model experiments and applications, the wavenumber vector azimuthal angle θ_0 is divided into 12, 16, or 20 equal sectors. In addition to simplicity (eliminating one set of the tuning parameters in the parameterization scheme), there are several physical justifications for an isotropic spectrum: (i) waves with small phase speed with random background wind will climatologically dominate the topographic gravity waves at the lower boundary; (ii) waves induced by convection (e.g., Alexander et al. 1995) or by geostrophic adjustment forced by a local momentum source (e.g., Zhu and Holton 1987) show near isotropic distribution in perturbation geopotential; and most importantly (iii) the gravity wave source spectrum added to the model will not change its dynamical property of conserving the total angular momentum. Note from Eq. (15) that there exists a difference in definition of the isotropic spectrum between the geopotential variance Φ_0^2 and momentum flux F_p . However, the first two justifications described above (i.e., small c with random U and large c with small U) also lead to an isotropic distribution in F_p .

We assume a wide range of horizontal wavenumber with 12 equally spaced sectors in logarithmic scale between $2\pi/(800 \text{ km})$ and $2\pi/(6.25 \text{ km})$. This logarithmic range is the same as the one used by Alexander (1998) in a modeling study of linear wave ray tracing that reproduces several climatological patterns observed for stratospheric gravity wave variance. Such a setting incorporates several well-known observational and modeling facts about gravity waves: (i) the characteristic wavelengths of the terrain-generated gravity waves are on the order of a few to tens of kilometers (e.g., Nappo 2002); (ii) the dominant wavelengths of the convectively generated gravity vary with period and range from tens to hundreds of kilometers (e.g., Alexander 1996); (iii) the typical horizontal wavelength generated by geostrophic adjustment under a localized momentum forcing is about 300 km (Zhu and Holton 1987); and (iv) increasing the horizontal wavelength reduces z_b (Alexander and Dunkerton 1999), which allows for a deeper and more uniform distribution of the parameterized drag and eddy diffusion. We also note that the typical horizontal resolution of current GCMs is on the order of hundreds of kilometers. The specification of the phase speed

spectrum $B_2(c, K)$ follows Matsuno (1982), Alexander and Dunkerton (1999), and most modeling studies that use a Gaussian function to construct the spectrum:

$$B_2(c, K) = \sum_j W_j \exp\left[-\left(\frac{c - c_{0j}}{c_{w,j}}\right)^2\right], \quad (36)$$

where the central phase speed c_{0j} , half-width $c_{w,j}$, and the corresponding weight W_j for different horizontal wavenumber K_j ($j = 1, \dots, 12$) are specified according to various observational and modeling constraints. Because the direction of the wave propagation has been represented by the wavenumber vector direction θ_0 , both c and K are positive. In the default setting, the phase speed is divided equally into 16 sectors between 5 and 70 m s^{-1} , with c_{0j} and $c_{w,j}$ varying linearly within $[0, 50]$ and $[10, 20]$, respectively. Computationally, the default setting of the three wave parameters consists of 20 equal sectors in θ_0 , 16 intervals in c , and 12 equally spaced sectors in logarithmic scale in K . Therefore, the source spectrum contains 3840 waves ($=20 \times 16 \times 12$). Most of these waves will break at different altitude levels to produce smooth profiles for the source terms in Eqs. (1)–(3).

The entire spectrum is normalized by the measurements based on the total variance of the gravity wave geopotential Φ_0^2 at the lower boundary, which varies with space and time and is constrained by the observational climatology. To give an estimate of its magnitude, we note that the variance of the geopotential height for planetary waves at 250-hPa in mid- and high-latitude regions is about 100–200 m (e.g., James 1994). If we assume that the variance of the geopotential height for gravity waves at the lower boundary is two orders of magnitude smaller than that of the planetary waves at the troposphere, then Φ_0^2 is on the order of $(10)^2 (\text{m}^2 \text{ s}^{-2})^2$ or $(20)^2 (\text{m}^2 \text{ s}^{-2})^2$. In Alexander and Dunkerton (1999), it is suggested that over topography, the magnitude of the observed pseudomomentum flux $\rho_0 \overline{u'w'}$ is 0.03 – 0.5 Pa. From Eq. (15), the variance of the corresponding geopotential is

$$\Phi_0^2 \approx \frac{2N|c - U_0 \cos\theta|}{\rho_{00}K} F_{p0} \sim 500 (\text{m}^2 \text{ s}^{-2})^2 \quad (37)$$

for a typical setting of $N = 0.02 \text{ s}^{-1}$, $\rho_{00} = 1.29 \text{ kg m}^{-3}$ at the surface, $|c - U_0 \cos\theta| = 20 \text{ m s}^{-1}$, and $K = 2\pi/(100 \text{ km})$, which is consistent with the above estimate scaled according to the planetary wave activity in the troposphere.

3. Numerical results of the parameterization scheme

A set of output fields near the Northern Hemisphere solstice (20050105) from version 5 of the Goddard Earth

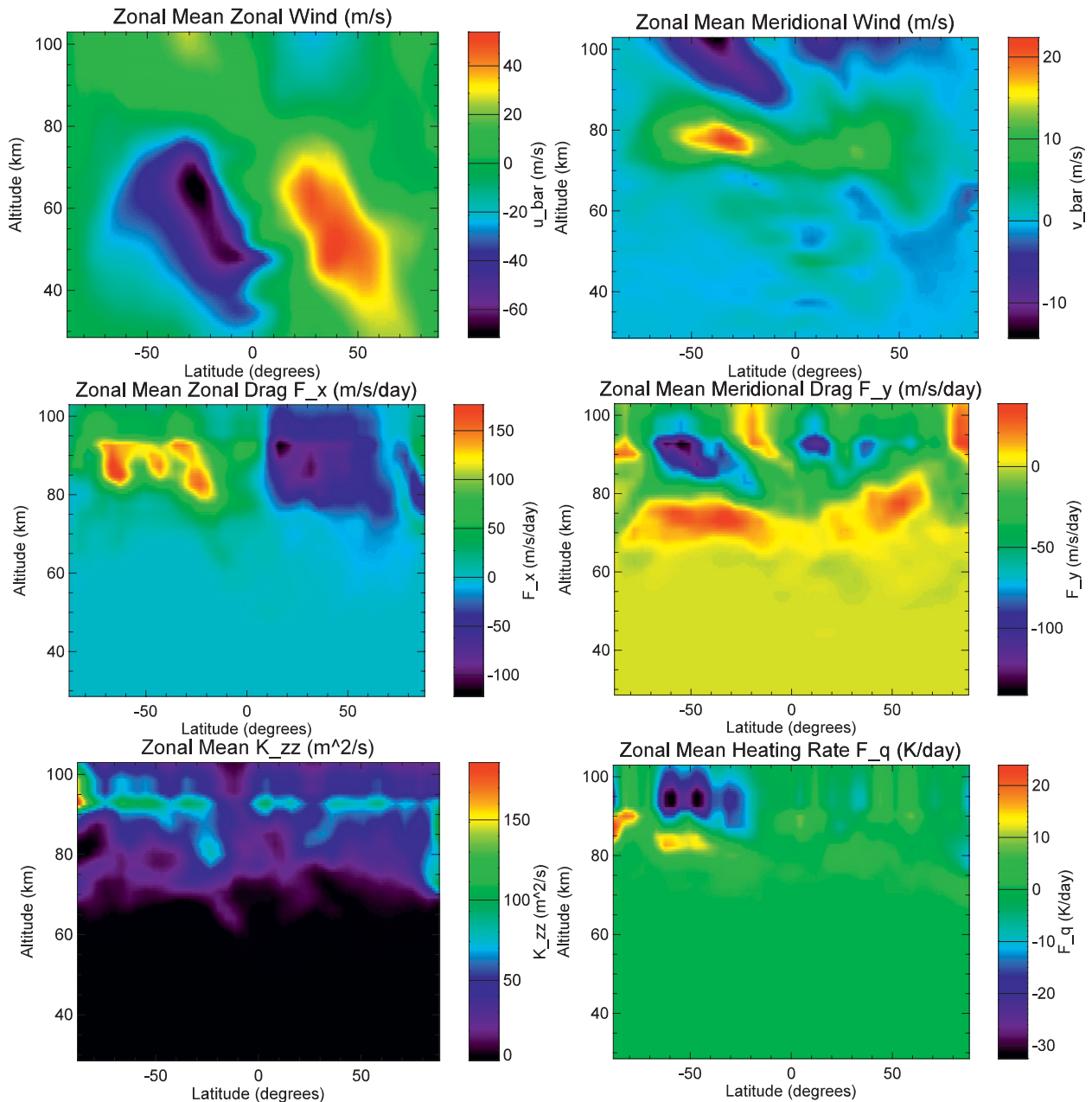


FIG. 1. Example of the winds from a high-altitude version of the GEOS-5 model (20050105) and the parameterized breaking gravity wave drag, eddy diffusion coefficient, and wave heating by gravity wave breaking from the GEOS-5 model runs near the NH winter solstice. All fields have been zonally averaged over 144 longitudinal grids: (top left) zonal and (top right) meridional wind; (middle left) zonal and (middle right) meridional drag; and (bottom left) eddy diffusion coefficient and (bottom right) heating rate.

Observing System Data Assimilation System (GEOS-5 DAS) is used to test the parameterization scheme. The GEOS-5 atmospheric GCM is a weather-climate-capable model consisting of a finite-volume dynamical core and a physical package parameterizing four major groups of physical processes (Rienecker et al. 2008). The standard setting of the atmospheric model has 72 vertical layers extending from the surface to ~ 70 km. The major physical

processes contained in the model are (i) moist processes including cloud microphysics, (ii) shortwave and infrared radiation, (iii) drag and eddy diffusion parameterized by a 2D Lindzen-type of scheme for gravity wave breaking (McFarlane 1987; Garcia 1991), and (iv) surface processes in the atmospheric boundary layer. A high-altitude version of the GEOS-5 atmospheric model has 82 vertical levels extending from the surface to ~ 100 km with

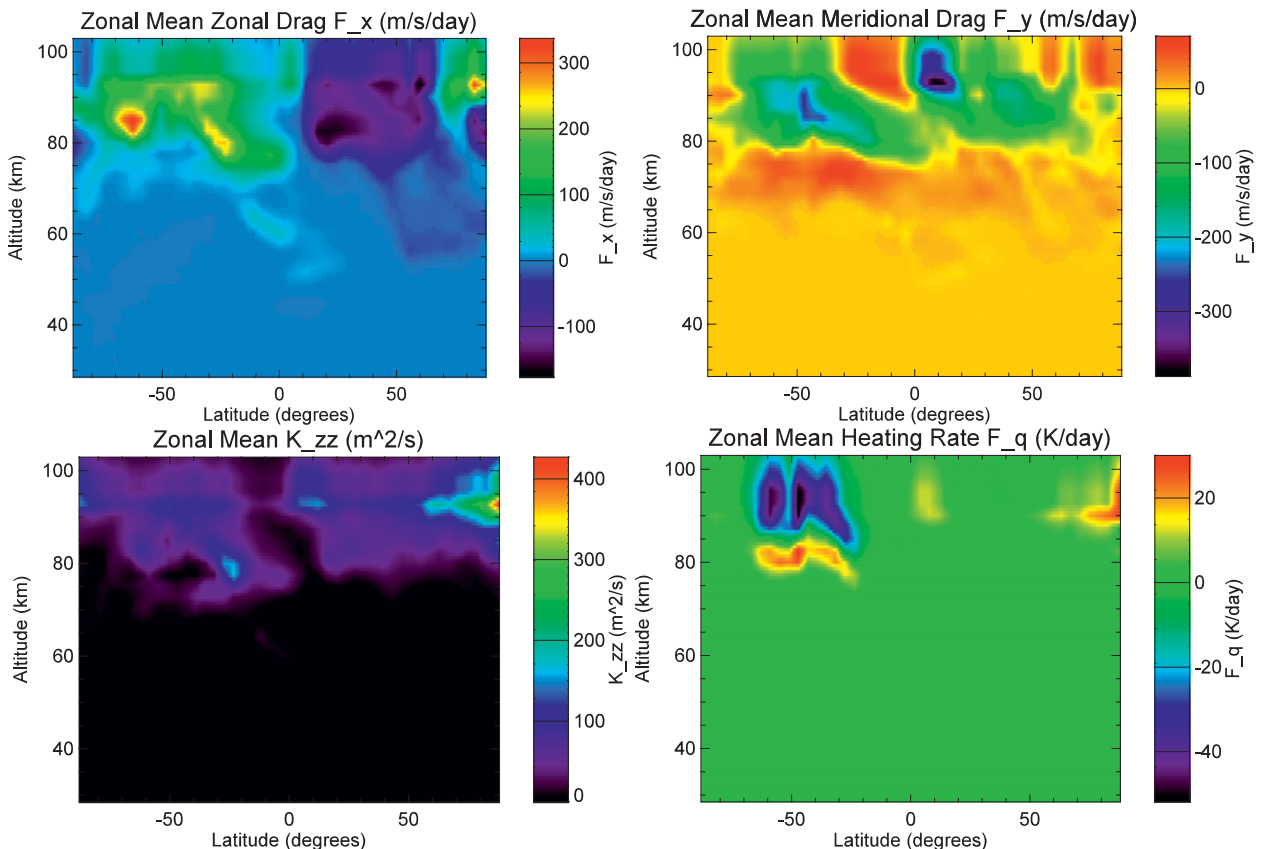


FIG. 2. Example of the parameterized breaking trinity: wave drag, eddy diffusion coefficient, and wave heating by gravity wave breaking derived from the zonally averaged wind and temperature fields near the NH winter solstice: (top left) zonal and (top right) meridional drag; and (bottom left) eddy diffusion coefficient and (bottom right) heating rate.

a horizontal resolution of 2.5° longitude by 2° latitude. In Fig. 1, we show the zonal mean fields of the assimilated model winds and the parameterized breaking trinity calculated by the current scheme based on the output model winds: wave drag, eddy diffusion coefficient, and wave heating by gravity wave breaking. We do not show the temperature field in the figure because it only plays a minor role in the parameterization scheme by modifying the background static stability. Note that the magnitudes of the zonal mean zonal drag \bar{S}_u and eddy diffusion coefficient \bar{K}_{zz-m} around the mesopause are comparable to those in previous studies based on traditional Lindzen-type gravity wave parameterizations, which were required to produce the horizontal anomalous temperature gradient (or the vertical zonal wind reversals) near the solstice mesopause (e.g., Holton 1983). In addition, the current 3D parameterization scheme also provides the forcing components of the meridional wave drag \bar{S}_v and wave heating rate \bar{S}_T in the primitive Eqs. (1)–(3). Near the mesopause, the overall magnitude of the wave heating and cooling due to wave breaking is comparable to other estimates based on energy dissipation rates either

from the model (e.g., Liu 2000; Becker and Schmitz 2002) or from the measurements (e.g., Lübken 1997) and is also comparable to the radiative and chemical heating rates in the same region (Zhu 1994; Zhu et al. 2000). In Liu (2000), the vertical wave heating rate distribution also shows some cancellation in altitude. Note that the added wave heating \bar{S}_T not only directly changes the thermal structure near the mesopause but also modifies the meridional circulation through its thermal drive of the meridional gradient of the heating rate (e.g., Zhu et al. 2001). Historically, parameterizations of \bar{S}_u and \bar{K}_{zz-m} by wave breaking were proposed to explain the observed large-scale features of the horizontal anomalous temperature gradient (or the vertical zonal wind reversals) near the solstice mesopause. Since \bar{S}_v and \bar{S}_T have been self-consistently derived together with \bar{S}_u and \bar{K}_{zz-m} , their additional effects on middle atmosphere dynamics and physics should also be an important subject to be carefully examined. It should be emphasized that all terms \bar{S}_u , \bar{S}_v , \bar{K}_{zz-m} , and \bar{S}_T have been consistently calculated on each model grid simultaneously for the corresponding individual input wind and temperature profiles. The 2D

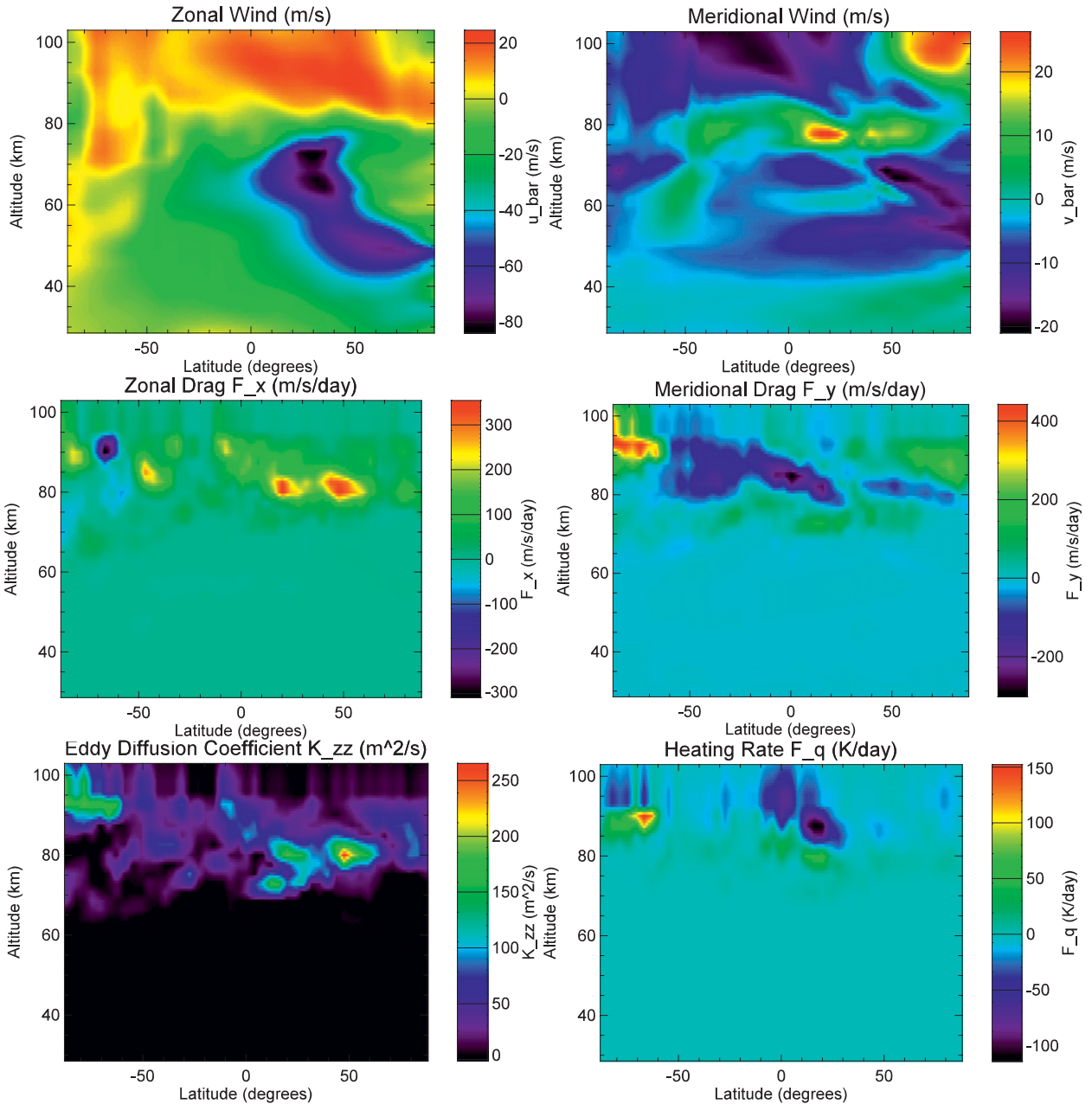


FIG. 3. As in Fig. 1, but on a longitudinal plane of 110°E, where the meridional wind is peaked.

plots shown in Fig. 1 represent the zonal mean fields averaged over 144 longitudinal grids.

Figure 2 shows the breaking trinity of \bar{S}_u , \bar{S}_v , \bar{K}_{zz-m} , and \bar{S}_T as a function of latitude and altitude calculated based on the zonally averaged wind field as shown on the top row of Fig. 1 and the corresponding averaged temperature field. Note that the wave-mean flow interactions as described in the last section by Eqs. (19), (23), and (26)–(30) are highly nonlinear. Therefore, the consequences of the breaking trinity calculated based on a

zonally averaged flow will not be the same as those shown in Fig. 1, which were calculated by zonally averaging the derived force terms. Specifically, the overall magnitudes in Fig. 2 are significantly greater than those in Fig. 1. However, a careful comparison of the two figures shows that they have similar spatial patterns. For example, near the solstice mesopause, the zonal momentum drag is mostly easterly in the winter hemisphere and westerly in the summer hemisphere, which is dynamically required to produce the horizontal anomalous temperature gradient

near the solstice mesopause. In addition, distribution of the wave heating \overline{S}_T shows well-organized dipole patterns with cooling regions sitting above the heating regions in both figures, as expected from its parameterization scheme (30). Physically, the existence of these differences and commonalities between the two sets of mean fields is not surprising because the zonal mean state in a 3D numerical model is driven somewhat differently than the one in a 2D model since they have entirely different subgrid scales.

The wind distribution at a particular longitude sector could significantly deviate from its zonal average. This is similar to the case in which a measured single wind profile at a prescribed location could be completely different than its climatology. To see such an effect and further illustrate the 3D nature of the current parameterization scheme, we show in Fig. 3 the input wind field (u, v) and the output force terms $(S_u, S_v, \overline{K}_{zz-m}, S_T)$ on a longitudinal plane (110°E) where the meridional wind is peaked. Comparison of Figs. 1 and 3 shows that both the input and output fields have significant differences in their magnitudes and patterns. Specifically, the zonal winds in the winter hemisphere around the stratopause are of opposite signs. As a result, the zonal drag force near the winter mesopause also changes sign because of the filtering effect of the upward-propagating gravity waves. Since the wave filtering effect is believed to be one of the main driving mechanisms for a variety of middle atmosphere circulations (e.g., Dunkerton 1982; Smith 1996; Mayr et al. 1998), the spectral parameterization of wave breaking proposed in the current paper is expected to be appropriate for simulations of various middle atmospheric circulations.

4. Conclusions

In this paper, we have developed a 3D spectral parameterization scheme to self-consistently include the “breaking trinity” of upward-propagating gravity waves for large-scale numerical models: (i) momentum drag that represents the nonlocalized transport of momentum through wave propagation in a 3D background flow, (ii) eddy diffusion coefficients that characterize the localized diffusive transport of momentum, heat, and tracers due to 3D mixing induced by wave breaking, and (iii) wave heating rate that captures localized transport of heat by perturbing wave structures to redistribute the thermal energy within a finite domain. For a set of given input wind and temperature profiles at each model grid (u, v, T) , the parameterization scheme returns five vertical profiles $S_u, S_v, \overline{K}_{zz-m}, \overline{K}_{zz-T}$, and S_T for calculating the force terms on the right-hand sides of the momentum and energy Eqs. (1)–(3).

The spectral parameterization has been developed by using a general relationship between the wave action flux and the wave momentum and heat fluxes developed by Zhu (1987) and a mapping approximation between the wave source spectrum and the vertical distribution of the momentum deposition developed by Alexander and Dunkerton (1999). When the parameterization algorithm is applied to a set of 3D wind fields output from a high-altitude version of the GEOS-5 atmospheric model, the derived zonal mean drag and eddy diffusion coefficient near the solstice mesopause are comparable to those derived in previous work and are required to produce the horizontal anomalous temperature gradient and the vertical zonal wind reversals near the solstice mesopause (e.g., Holton 1983). The derived wave heating and cooling rates near the mesopause are found to be 10–20 K day⁻¹, which is comparable to the radiative and chemical heating rates. The filtering effect of the upward-propagating gravity waves is also well captured by the current parameterization scheme.

Acknowledgments. The authors wish to thank two anonymous reviewers for helpful comments on the original manuscript. Xun Zhu wishes to thank Hans G. Mayr for helpful discussions and suggestions in this study. This research was supported by the TIMED project sponsored by NASA under Contract NAS5-97179, NASA Grants NNG05GG57G and NNX09AH77G, and in part by NSF Grants ATM-0730158 and ATM-0640864 to The Johns Hopkins University Applied Physics Laboratory.

REFERENCES

- Akmaev, R. A., 1997: Optimization of a middle atmosphere diagnostic scheme. *J. Atmos. Sol.-Terr. Phys.*, **59**, 983–992.
- , 2007: On the energetics of mean-flow interactions with thermally dissipating gravity waves. *J. Geophys. Res.*, **112**, D11125, doi:10.1029/2006JD007908.
- Alexander, M. J., 1996: A simulated spectrum of convectively generated gravity waves: Propagation from the tropopause to the mesopause and effects on the middle atmosphere. *J. Geophys. Res.*, **101**, 1571–1588.
- , 1998: Interpretations of observed climatological patterns in stratospheric gravity wave variance. *J. Geophys. Res.*, **103** (D8), 8627–8640.
- , and T. J. Dunkerton, 1999: A spectral parameterization of mean-flow forcing due to breaking gravity waves. *J. Atmos. Sci.*, **56**, 4167–4182.
- , J. R. Holton, and D. R. Durran, 1995: The gravity wave response above deep convection in a squall line simulation. *J. Atmos. Sci.*, **52**, 2212–2226.
- Andrews, D. G., J. R. Holton, and C. B. Leovy, 1987: *Middle Atmosphere Dynamics*. Academic Press, 489 pp.
- Becker, E., 2004: Direct heating rates associated with gravity wave saturation. *J. Atmos. Sol.-Terr. Phys.*, **66**, 683–696.
- , 2009: Sensitivity of the upper mesosphere to the Lorenz energy cycle of the troposphere. *J. Atmos. Sci.*, **66**, 647–666.

- , and G. Schmitz, 2002: Energy deposition and turbulent dissipation owing to gravity waves in the mesosphere. *J. Atmos. Sci.*, **59**, 54–68.
- Broutman, D., J. W. Rottman, and S. D. Eckermann, 2001: A hybrid method for wave propagation from a localized source, with application to mountain waves. *Quart. J. Roy. Meteor. Soc.*, **127**, 129–146.
- , —, and —, 2002: Maslov's method for stationary hydrostatic mountain waves. *Quart. J. Roy. Meteor. Soc.*, **128**, 1159–1171.
- , —, and —, 2004: Ray methods for internal waves in the atmosphere and ocean. *Annu. Rev. Fluid Mech.*, **36**, 233–253.
- Chao, W. C., and M. R. Schoeberl, 1984: On the linear approximation of gravity wave saturation in the mesosphere. *J. Atmos. Sci.*, **41**, 1893–1898.
- Dunkerton, T. J., 1981: Wave transience in a compressible atmosphere. Part I: Transient internal wave, mean-flow interaction. *J. Atmos. Sci.*, **38**, 281–297.
- , 1982: Theory of the mesopause semiannual oscillation. *J. Atmos. Sci.*, **39**, 2681–2690.
- , 1984: Inertia-gravity waves in the stratosphere. *J. Atmos. Sci.*, **41**, 3396–3404.
- Dutton, J. A., 1976: *The Ceaseless Wind*. McGraw-Hill, 579 pp.
- Eckermann, S. D., 1992: Ray-tracing simulation of the global propagation of inertia gravity waves through the zonally averaged middle atmosphere. *J. Geophys. Res.*, **97**, 15 849–15 866.
- Fritts, D. C., 1984: Gravity wave saturation in the middle atmosphere: A review of theory and observations. *Rev. Geophys. Space Sci.*, **22**, 275–308.
- , 1995: Gravity wave-tidal interactions in the middle atmosphere: Observations and theory. *The Upper Mesosphere and Lower Thermosphere: A Review of Experiment and Theory*, *Geophys. Monogr.*, Vol. 87, Amer. Geophys. Union, 121–131.
- , and P. K. Rastogi, 1985: Convective and dynamical instabilities due to gravity wave motions in the lower and middle atmosphere: Theory and observations. *Radio Sci.*, **20**, 1247–1277.
- Garcia, R. R., 1991: Parameterization of planetary wave breaking in the middle atmosphere. *J. Atmos. Sci.*, **48**, 1405–1419.
- Hines, C. O., 1960: Internal atmospheric gravity waves at ionospheric heights. *Can. J. Phys.*, **38**, 1441–1481.
- Hirota, I., and T. Niki, 1985: A statistical study of inertia-gravity waves in the middle atmosphere. *J. Meteor. Soc. Japan*, **63**, 1055–1066.
- Holton, J. R., 1975: *The Dynamic Meteorology of the Stratosphere and Mesosphere*. *Meteor. Monogr.*, No. 37, Amer. Meteor. Soc., 218 pp.
- , 1982: The role of gravity wave induced drag and diffusion in the momentum budget of the mesosphere. *J. Atmos. Sci.*, **39**, 791–799.
- , 1983: The influence of gravity wave breaking on the general circulation of the middle atmosphere. *J. Atmos. Sci.*, **40**, 2497–2507.
- , and R. S. Lindzen, 1972: An updated theory for the quasi-biennial cycle of the tropical stratosphere. *J. Atmos. Sci.*, **29**, 1076–1080.
- , and X. Zhu, 1984: A further study of gravity wave induced drag and diffusion in the mesosphere. *J. Atmos. Sci.*, **41**, 2653–2662.
- , and M. J. Alexander, 2000: The role of waves in the transport circulation of the middle atmosphere. *Atmospheric Science across the Stratopause*, *Geophys. Monogr.*, Vol. 123, Amer. Geophys. Union, 21–35.
- James, I. N., 1994: *Introduction to Circulating Atmospheres*. Cambridge University Press, 422 pp.
- Lieberman, R. S., and P. B. Hays, 1994: An estimate of the momentum deposition in the lower thermosphere by the observed diurnal tide. *J. Atmos. Sci.*, **51**, 3094–3105.
- Lighthill, M. J., 1978: *Waves in Fluids*. Cambridge University Press, 504 pp.
- Lindzen, R. S., 1974: Stability of a Helmholtz velocity profile in a continuously stratified, infinite Boussinesq fluid—Applications to clear air turbulence. *J. Atmos. Sci.*, **31**, 1507–1514.
- , 1981: Turbulence and stress owing to gravity wave and tidal breakdown. *J. Geophys. Res.*, **86**, 9707–9714.
- Liu, H.-L., 2000: Temperature changes due to gravity wave saturation. *J. Geophys. Res.*, **105**, 12 329–12 336.
- Lorenz, E. N., 1955: Available potential energy and the maintenance of the general circulation. *Tellus*, **7**, 157–167.
- Lübken, F.-J., 1997: Seasonal variation of turbulent energy dissipation rates at high latitudes as determined by in situ measurements of neutral density fluctuations. *J. Geophys. Res.*, **102** (D12), 13 441–13 456.
- Marks, C. J., and S. D. Eckermann, 1995: A three-dimensional nonhydrostatic ray-tracing model for gravity waves: Formulation and preliminary results for the middle atmosphere. *J. Atmos. Sci.*, **52**, 1959–1984.
- Matsuno, T., 1970: Vertical propagation of stationary waves in the winter northern hemisphere. *J. Atmos. Sci.*, **27**, 871–883.
- , 1982: A quasi-one-dimensional model of the middle-atmosphere circulation interacting with internal gravity waves. *J. Meteor. Soc. Japan*, **60**, 215–226.
- Mayr, H. G., J. G. Mengel, K. L. Chan, and H. S. Porter, 1998: Seasonal variations of the diurnal tide induced by gravity wave filtering. *Geophys. Res. Lett.*, **25**, 943–946.
- McFarlane, N. A., 1987: The effect of orographically excited gravity wave drag on the general circulation of the lower stratosphere and troposphere. *J. Atmos. Sci.*, **44**, 1775–1800.
- McIntyre, M., 2000: On global-scale atmospheric circulation. *Perspectives in Fluid Dynamics—A Collective Introduction to Current Research*, G. K. Batchelor, H. K. Moffatt, and M. G. Worster, Eds., Cambridge University Press, 557–624.
- Mlynczak, M. G., and D. K. Zhou, 1998: Kinetic and spectroscopic requirements for the measurement of mesospheric ozone at 9.6 μm under non-LTE conditions. *Geophys. Res. Lett.*, **25**, 639–642.
- Nappo, C. J., 2002: *An Introduction to Atmospheric Gravity Waves*. Academic Press, 276 pp.
- Palmer, T. N., 1982: Properties of the Eliassen–Palm flux for planetary scale motions. *J. Atmos. Sci.*, **39**, 992–997.
- Pope, S. B., 2000: *Turbulent Flow*. Cambridge University Press, 771 pp.
- Rienecker, M., and Coauthors, 2008: The GEOS-5 data assimilation system—Documentation of Versions 5.0.1, 5.1.0, and 5.2.0. National Aeronautics and Space Administration Rep. NASA/TM-2008-104606, Vol. 27, 101 pp.
- Sato, K., 1994: A statistical study of the structure, saturation and sources of inertia-gravity waves in the lower stratosphere observed with the MU radar. *J. Atmos. Terr. Phys.*, **56**, 755–774.
- Scinocca, J. F., and R. Ford, 2000: The nonlinear forcing of large-scale internal gravity waves by stratified shear instability. *J. Atmos. Sci.*, **57**, 653–672.
- Shaw, T. A., and T. G. Shepherd, 2009: A theoretical framework for energy and momentum consistency in subgrid-scale parameterization for climate models. *J. Atmos. Sci.*, **66**, 3095–3114.
- Smith, A. K., 1996: Longitudinal variations in mesospheric winds: Evidence for gravity wave filtering by planetary waves. *J. Atmos. Sci.*, **53**, 1156–1173.

- Strobel, D. F., 1989: Constraints on gravity wave induced diffusion in the middle atmosphere. *Pure Appl. Geophys.*, **130**, 533–546.
- , M. E. Summers, R. M. Bevilacqua, M. T. DeLand, and M. Allen, 1987: Vertical constituent transport in the mesosphere. *J. Geophys. Res.*, **92** (D6), 6691–6698.
- Talaat, E. R., J.-H. Yee, and X. Zhu, 2001: Gravity wave feedback effects on the diurnal migrating tide. *Adv. Space Res.*, **27**, 1755–1760.
- Teixeira, M. A. C., P. M. A. Miranda, and M. A. Valente, 2004: An analytical model of mountain wave drag for wind profiles with shear and curvature. *J. Atmos. Sci.*, **61**, 1040–1054.
- Tennekes, H., and J. L. Lumley, 1972: *A First Course in Turbulence*. MIT Press, 300 pp.
- Walterscheid, R. L., 1981: Dynamical cooling induced by dissipating internal gravity waves. *Geophys. Res. Lett.*, **8**, 1235–1238.
- Warner, C. D., and M. E. McIntyre, 1996: On the propagation and dissipation of gravity wave spectra through a realistic middle atmosphere. *J. Atmos. Sci.*, **53**, 3213–3235.
- Yamanaka, M. D., and H. Tanaka, 1984: Propagation and breakdown of internal inertio-gravity waves near critical levels in the middle atmosphere. *J. Meteor. Soc. Japan*, **62**, 1–17.
- Zhu, X., 1987: On gravity wave–mean flow interactions in a three-dimensional stratified atmosphere. *Adv. Atmos. Sci.*, **4**, 287–299.
- , 1994: An accurate and efficient radiation algorithm for middle atmosphere models. *J. Atmos. Sci.*, **51**, 3593–3614.
- , 2004: Radiative transfer in the middle atmosphere and planetary atmospheres. *Observation, Theory, and Modeling of Atmospheric Variability*, X. Zhu et al., Eds., World Scientific, 359–396.
- , and J. R. Holton, 1987: Mean fields induced by local gravity-wave forcing in the middle atmosphere. *J. Atmos. Sci.*, **44**, 620–630.
- , Z. Shen, S. D. Eckermann, M. Bittner, I. Hirota, and J.-H. Yee, 1997: Gravity wave characteristics in the middle atmosphere derived from the empirical mode decomposition method. *J. Geophys. Res.*, **102** (D14), 16 545–16 561.
- , J.-H. Yee, and D. F. Strobel, 2000: Coupled models of photochemistry and dynamics in the mesosphere and lower thermosphere. *Atmospheric Science across the Stratopause*, *Geophys. Monogr.*, Vol. 123, Amer. Geophys. Union, 337–342.
- , —, and E. R. Talaat, 2001: Diagnosis of dynamics and energy balance in the mesosphere and lower thermosphere. *J. Atmos. Sci.*, **58**, 2441–2454.
- , —, —, M. Mlynczak, L. Gordley, C. Mertens, and J. M. Russell III, 2005: An algorithm for extracting zonal mean and immigrating tidal fields in the middle atmosphere from satellite measurements: Applications to TIMED/SABER-measured temperature and tidal modeling. *J. Geophys. Res.*, **110**, D02105, doi:10.1029/2004JD004996.
- , —, and —, 2007: Effect of dynamical–photochemical coupling on oxygen airglow emission and implications for daytime ozone retrieved from 1.27 μm emission. *J. Geophys. Res.*, **112**, D20304, doi:10.1029/2007JD008447.
- , —, —, M. Mlynczak, and J. M. Russell III, 2008: Diagnostic analysis of tidal winds and the Eliassen–Palm flux divergence in the mesosphere and lower thermosphere from TIMED/SABER temperatures. *J. Atmos. Sci.*, **65**, 3840–3859.